RESEARCH ARTICLE

Energy & Environmental Materials WILEY

CO$_2$ Electrochemical Reduction

Flow-Through Hollow Fiber Gas Diffusion Electrodes with Morphology-Controlled In Situ Galvanic Grown Silver Catalysts for Enhanced CO Selectivity in CO$_2$ Electroreduction

Guoliang Chen, Beibei Ma, Yizhu Kuang, Hesamoddin Rabiee, Fatereh Dorosti, Ashok Kumar Nanjundan, Zhonghua Zhu, Hao Wang, and Lei Ge**

Electrochemical reduction of CO$_2$ (CO$_2$RR) into value-added products offers a promising strategy to reduce dependence on fossil fuels, particularly when powered by renewable electricity. However, CO$_2$RR faces challenges, including high activation energy barriers, competing side reactions, and limited CO$_2$ mass transport. Addressing these limitations requires not only the development of advanced electrocatalysts to enhance CO$_2$RR activity but also the design of electrodes to optimize gas-catalyst-electrolyte interfaces and facilitate efficient mass transport, thereby advancing CO$_2$RR toward industrial-scale applications. Herein, we developed flow-through hollow fiber gas diffusion electrodes (HFGDEs) featuring in situ galvanic growth of flower-like silver structures. The abundant ultrathin 2D nanosheets enhance active sites and CO$_2$RR activity, and the resulting electrode achieves a high Faradaic efficiency of CO of 91% at −1.2 (V vs RHE). Furthermore, the HFGDE configuration ensured sufficient CO$_2$ delivery to the active sites, enabling a partial current density of CO of 280.8 mA cm^{-2}. In situ Raman spectroscopy revealed that the in situ-grown silver flower structure promotes the adsorption of *COOH intermediate, thereby accelerating CO$_2$RR kinetics. Moreover, the robust CO$_2$ supply afforded by the HFGDE configuration is crucial to suppress competitive hydrogen evolution reaction (HER) and maintain high CO$_2$RR activity under industrially relevant current densities.

1. Introduction

The excessive reliance on fossil fuels has led to a sharp rise in atmospheric CO$_2$ concentrations, intensifying the greenhouse effect and accelerating global climate change.[1,2] This pressing issue necessitates the development of efficient strategies for CO$_2$ capture, storage, and conversion.[3,4] Among these, the electrochemical reduction reaction of CO$_2$ (CO$_2$RR), powered by renewable electricity, has emerged as a promising route for converting CO$_2$ into value-added products such as carbon monoxide (CO), formic acid, and alcohols.[5–10] CO is particularly attractive due to its industrial relevance as a key feedstock in processes like Fischer–Tropsch synthesis.[11] However, achieving high selectivity and activity for CO production is challenging, primarily due to the competitive hydrogen evolution reaction (HER) and the substantial energy barrier associated with CO$_2$ activation.[12–14]

In addition to the development of efficient electrocatalysts, the design of advanced electrode architecture is critical, particularly for overcoming CO$_2$ mass transport limitations in the conventional H-cell system under industrial current density.[15,16] Gas diffusion electrodes (GDEs), integrated into flow-cell configurations, are now standard for evaluating catalyst performance at high reaction rates.[17] Conventional GDEs typically comprise multiple layers, including a gas diffusion layer, microporous layers, and a catalyst layer, where the catalysts are dispersed with polymeric binders (e.g, Nafion ionomer and PTFE) and coated onto a carbon substrate.[18,19] In contrast, self-supported hollow fiber gas diffusion electrodes (HFGDEs) can simplify cell structure by utilizing the lumen side as a gas chamber. CO$_2$ gas is directly fed through the lumen side of the hollow fiber, where it penetrates through the hollow fiber walls to reach active sites, ensuring sufficient CO$_2$ delivery at the triple-phase interfaces.[20,21]

Copper hollow fibers (Cu HFs) have proven particularly effective for microtubular GDEs in the application of CO$_2$ electrochemical conversion. Pristine Cu HF typically produces a mixture of products, such as CO, formate, and C$_{2+}$ hydrocarbons, due to its broad catalytic behavior at varying current density.[22–26] Moreover, copper hollow fiber can

---

Dr. G. Chen, Dr. Y. Kuang, Dr. F. Dorosti, Prof. A. K. Nanjundan, Prof. H. Wang, Prof. L. Ge
Centre for Future Materials, University of Southern Queensland, Springfield, Queensland 4300, Australia
E-mail: hao.wang@usq.edu.au
E-mail: lei.ge@usq.edu.au
Dr. B. Ma, Dr. F. Dorosti, Prof. Z. Zhu
School of Chemical Engineering, The University of Queensland, Brisbane, Queensland 4072, Australia
Dr. H. Rabiee
Department of Chemistry, Biochemistry and Pharmaceutical Sciences, University of Bern, Freiestrasse 3, 3012, Bern, Switzerland
Prof. A. K. Nanjundan, Prof. H. Wang, Prof. L. Ge
School of Engineering, University of Southern Queensland, Springfield, Queensland 4300, Australia

The ORCID identification number(s) for the author(s) of this article can be found under https://doi.org/10.1002/eem2.70205.

DOI: 10.1002/eem2.70205

serve as conductive substrates for the in situ growth of electrocatalysts, allowing for precise control over product distribution.[27–33] For instance, modification with bismuth or tin has enhanced formate production,[30,31,33] while the deposition of zinc nanosheets has shown promise for syngas generation.[27] Among metallic catalysts, silver is regarded as one of the most selective catalysts for CO production. However, direct electrodeposition of Ag on Cu HF is complicated by spontaneous galvanic replacement reaction (GRR), due to the more positive standard reduction potential of Ag^+/Ag ($E^0_{Ag+/Ag} = +0.799$ V) compared to Cu^{2+}/Cu ($E^0_{Cu2+/Cu} = +0.34$ V).[28]

To address this, we present the rational design of HFGDEs incorporating in situ GRR-grown silver catalysts on Cu HF for efficient electrochemical conversion of CO_2 to CO at industrial-level current densities. The morphology of the Ag catalyst can be precisely tuned to dendritic structure (Ag DS-HF) or flower-like nanostructure (Ag FS-HF) by introducing citric acid and ammonia to modulate the nucleation and growth environment. The Ag FS-HF electrode exhibits a significantly enlarged electrochemical surface area (ECSA), which is nearly twice that of bare Cu HF, enhanced electron transport, and improved CO_2 accessibility at the triple-phase interface, effectively suppressing HER and promoting CO_2RR kinetics. Notably, the Ag FS-HF electrode achieved a high Faradaic efficiency of CO of 91.0% at −1.2 (V vs RHE), along with a partial current density of CO of 280.8 mA cm^{-2} under a total current density of 400 mA cm^{-2}. Furthermore, the ratio of partial current density of CO in GDE mode versus non-GDE mode increased significantly with current density, highlighting the essential role of CO_2 supply in suppressing HER and maintaining CO_2RR activity.

2. Results and Discussion

2.1. Microstructure and Morphology Analysis

The preparation of silver flower structure-based HFGDEs is schematically presented in **Figure 1a**. After immersing pre-treated Cu HF into different Ag GRR solutions, a rapid color change of the copper surface was observed, indicating a fast galvanic replacement reaction between Cu and Ag^+. The resulting fibers exhibited distinct morphologies and colors. The sample with dendritic silver morphology (Ag DS-HF) turned black (Figure 1b,c), while the one with flower structure (Ag FS-HF) appeared gray (Figure 1b,d). In contrast to the loosely bound dendritic silver structures on Ag DS-HF, the Ag FS-HF displayed a densely packed assembly of ultrathin nanosheets uniformly covering the Cu HF surface. Cross-sectional images of Ag FS-HF (Figure 1e,f) further confirm that the silver catalyst is predominantly localized on the outer surface of the hollow fiber, consistent with the energy dispersive spectroscopy (EDS) elemental mapping image of Ag FS-HF (Figure 1g).

The hollow fiber gas diffusion electrode was prepared by sticking a hollow fiber into a copper tube via conductive silver epoxy. The other ends as well as the joints were sealed and covered with non-conductive and gas-tight epoxy and tested in an H-cell setup (Figure S2a,b, Supporting Information). CO_2 gas penetrates through the hollow fiber walls (Cu skeleton) and reaches partially wetted silver catalysts (Figure S2c, Supporting Information). The effective surface area of the electrode is mostly the silver catalyst layer on the outside surface of the hollow fiber electrode. The thickness of silver catalysts with a flower structure is around 11.5 μm (Figure S3, Supporting Information).

The crystalline structures of Cu HF, Ag DS-HF, and Ag FS-HF were further characterized via X-ray diffraction (XRD). For the pristine Cu HF, characteristic peaks were observed at 43.3, 50.4, and 74.1°, corresponding to the (111), (200), and (220) crystal planes of metallic Cu (PDF#89-0838).[27] In both Ag-grown samples, the intensities of these Cu peaks decreased, particularly in Ag FS-HF, indicating significant surface coverage of Ag catalysts. In addition, four distinct peaks emerged at 38.2, 44.3, 64.4, and 77.5° (Figure 1h), corresponding to the Ag (111), (200), (220), and (311) crystal planes of the metallic Ag (PDF#87–0718).[28] To further investigate the surface element composition, X-ray photoelectron spectroscopy (XPS) was conducted. Ag FS-HF exhibited the highest Ag 3d signal and the lowest Cu 2p intensity among the samples (Figure S4, Supporting Information), consistent with the XRD findings. Quantitative XPS analysis revealed a surface atomic ratio of Ag to Cu for Ag FS-HF is 97.8:2.2, while Ag DS-HF retained a significantly higher Cu surface exposure, with 24.4% of Cu atoms presented on the outer surface (Table S1, Supporting Information). High-resolution XPS spectra of Ag 3d showed peaks at 374.3 and 368.3 eV, respectively, corresponding to Ag $3d_{3/2}$ and Ag $3d_{5/2}$,[34,35] characteristic of metallic Ag^0 (Figure 1i).

The growth mechanism of Ag catalysts on Cu HF was investigated in detail. The outer surface of the Cu HF, composed of micron-sized fused copper particles (**Figure 2a**), provides abundant active sites for the reduction of Ag^+ during GRR. Immersing Cu HF in a 0.02 M $AgNO_3$ solution for a few seconds initiates rapid nucleation, yielding dendritic and oversized Ag structures (Figure 2b), indicating an unregulated and rapid replacement reaction between Cu and Ag^+ ions.[36] To suppress this rapid reaction rate and promote controlled morphology, citrate ions were introduced as shape-directing agents, adsorbing onto the Ag (111) crystal facets and facilitating the anisotropic growth required for Ag nanosheet formation.[37–39] However, adding citric acid alone is insufficient to direct Ag nanosheet formation due to the limited availability of free citrate ions under weak acidic conditions (Figure 2c).

The formation of high-density Ag nanosheet-based flower-like structures on Cu HF was achieved through the synergistic action of citric acid and ammonia during the GRR between Ag^+ and Cu. Ammonia plays two essential roles: it promotes the deprotonation of citric acid, thereby increasing the concentration of free citrate ions, and it complexes with Ag^+ to form $[Ag(NH_3)_2]^+$, effectively moderating the reduction kinetics by lowering the concentration of free Ag^+ ions. Citrate is a tricarboxylate anion at near-neutral/basic pH. The deprotonated carboxyl groups strongly interact with the positively charged surface atoms of Ag(111) through electrostatic interactions and weak coordination. Because citrate stabilizes Ag(111), the growth rate along the [111] direction is suppressed, resulting in two-dimensional lateral growth and promoting the formation of ultrathin nanosheets rather than isotropic particles.[37]

The GRR solution was composed of 0.02 M $AgNO_3$ with citric acid at controlled molar ratios relative to Ag^+, followed by adding ammonia to form a transparent solution. Similar to the formation of $[Ag(NH_3)_2]^+$ solution, after adding ammonia to $AgNO_3$ with citric acid solution, the whitish precipitate Ag(OH) that forms initially redissolves with further addition of ammonia until forming a transparent solution. A systematic investigation of the Ag-to-citrate molar ratio revealed a strong dependence of morphology on the molar ratio. At a ratio of 8:1, smaller nanosheets dominate (Figure 2d), while decreasing the ratio to 4:1 and 2:1 results in progressively larger nanosheets (Figure 2e,f). When the ratio reached 1:1, the formation of bulky, agglomerated silver particles became apparent (Figure 2g). Further decreasing the ratio to 1:2 eliminates nanosheet formation, likely due

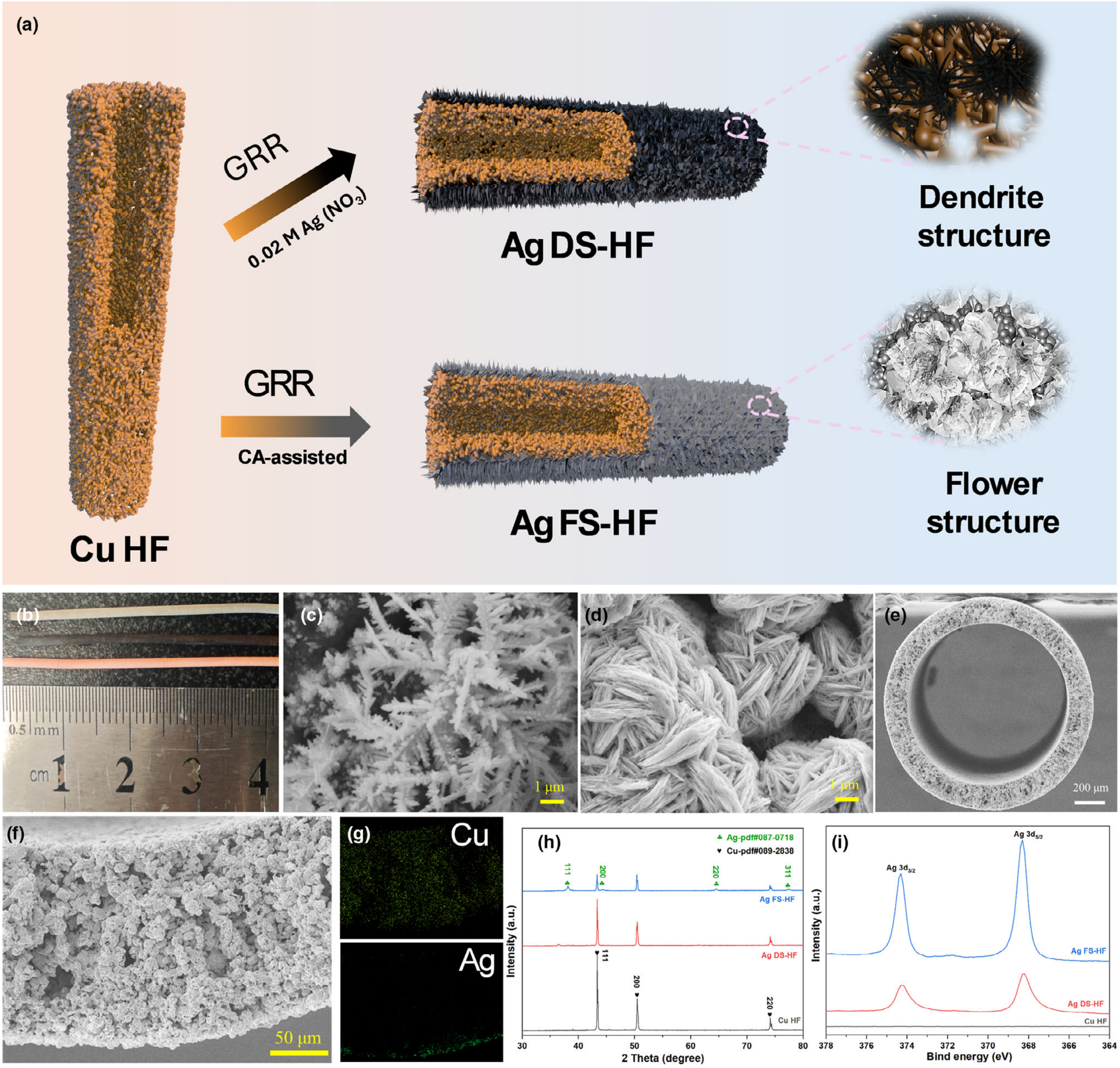

Figure 1. a) Schematic illustration of controlling growth silver catalysts with different morphologies on Copper hollow fiber via galvanic replacement methods; b) Photo images Cu HF, Ag DS-HF, Ag FS-HF; Surface SEM images of c) Ag DS-HF, and d) Ag FS-HF; Cross-sectional images of e) Ag FS-HF and f) Ag FS-HF with high magnification; g) energy dispersive spectroscopy (EDS) elemental mapping images of cross-sectional of Ag FS-HF; h) XRD patterns of Cu HF, Ag DS-HF, and Ag FS-HF; i) high-resolution XPS spectra of Ag 3d for Cu HF, Ag DS-HF, and Ag FS-HF.

to excessive citric acid shifting the equilibrium toward non-dissociated species and reducing the effective concentration of free citrate ions (Figure 2h). Ammonia also modulates the redox kinetics by complexing with Ag^+ to form $[Ag(NH_3)_2]^+$. When a 0.02 M $[Ag(NH_3)_2]^+$ solution was directly used in the GRR, the resulting Ag structures exhibited a nanoparticulate morphology on the Cu HF surface (Figure 2i), suggesting a slower reaction rate due to suppressed free Ag^+ ions, underscoring the dual role of ammonia as both a deprotonation promoter and a complexing agent.

To further validate the reproducibility and universality of the GRR procedure, both Cu foil and Cu mesh substrates were employed for the in situ growth of flower-like silver nanostructures via the GRR. After being placed in the GRR solution for 20 mins, the shiny copper color of both samples turned gray, indicating silver deposition. The surface SEM images of both samples before and after GRR confirmed the formation of abundant silver nanosheets distributed on the smooth surfaces of both Cu foil and Cu mesh (Figure S5, Supporting Information).

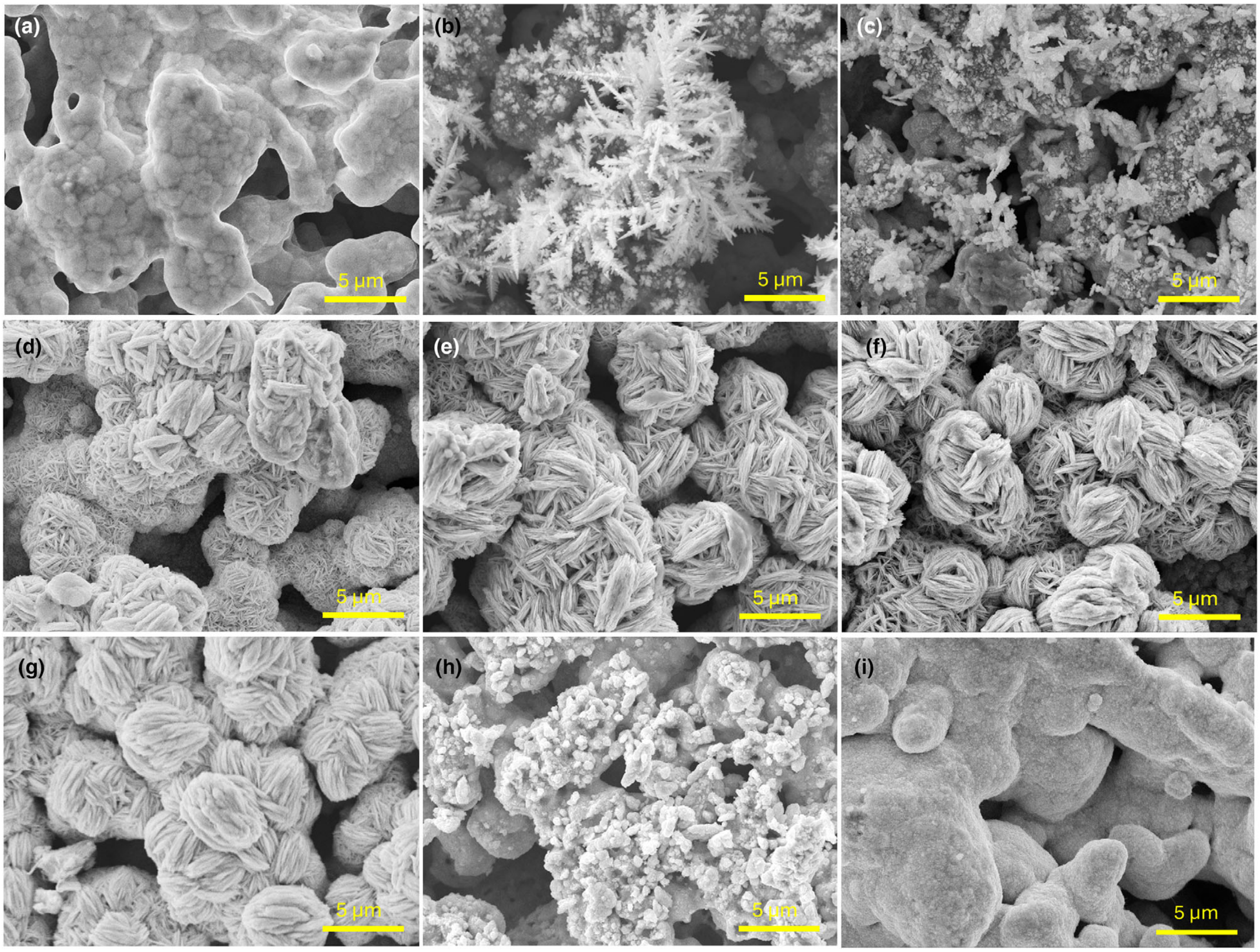

Figure 2. Surface SEM images of a) Cu HF, Cu HF after immersed in b) 0.02 M Ag NO_3, c) 0.02 M Ag NO_3 + 0.01 M critic acid (CA), d) 0.02 M Ag NO_3 + 0.0025 M CA + $NH_3 \cdot H_2O$, e) 0.02 M Ag NO_3 + 0.005 M CA + $NH_3 \cdot H_2O$, f) 0.02 M Ag NO_3 + 0.01 M CA + $NH_3 \cdot H_2O$, g) 0.02 M Ag NO_3 + 0.02 M CA + $NH_3 \cdot H_2O$, h) 0.02 M Ag NO_3 + 0.04 M CA + $NH_3 \cdot H_2O$, and i) 0.02 M $[Ag(NH_3)_2]^+$ solution.

The proposed mechanism for the formation of dense, flower-like silver structures is illustrated in Figure S6, Supporting Information. When immersing Cu HF in a galvanic solution containing Ag^+, citric acid, and ammonia, Ag^+ is reduced by electrons supplied by the metallic Cu to form Ag^0 nuclei. Citrate ions, facilitated by ammonia-mediated deprotonation, adsorb onto the Ag (111) crystal facets, directing the anisotropic growth of Ag nanosheets. Simultaneously, the presence of $[Ag(NH_3)_2]^+$ complexes modulates the local reduction kinetics, allowing for controlled nucleation and sheet growth. Cross-sectional SEM images (Figure S3a,b, Supporting Information) support this mechanism, revealing the formation of a compact layer of small Ag nanosheets followed by their lateral expansion into larger sheets and a flower structure.

2.2. Electrocatalytic CO_2RR Performance of HFGDEs

The electrocatalytic performance of HFGDEs was evaluated in a customized H-cell. As shown in **Figure** 3a, all hollow fiber electrodes exhibited increasing current densities with applied more negative potentials, indicating excellent electron transfer (ET) between electrodes and in situ grown catalysts. The Ag FS-HF electrode demonstrated nearly twice the current density of the bare Cu HF electrode, attributed to the presence of silver and its high-density nanosheet structure, which offers a greater ECSA (Figure 3a). This structural advantage resulted in a high intrinsic selectivity for CO production, with the Ag FS-HF electrode achieving more than 80% FE for CO (Figure 3b) across a potential window from −0.9 to −1.3 (V vs RHE). A peak CO FE of 91% was observed at −1.2 (V vs RHE). In contrast, the Cu HF electrode favored formate formation, with around 70% FE (Figure S7, Supporting Information) over the potential from −1 to −1.3 (V vs RHE), consistent with previous reports of Cu HF.[23,24] The Ag DS-HF exhibited a mixed product distribution of CO and formate, attributed to the co-exposure of Cu particles and Ag dendritic catalytic sites (Table S1, Supporting Information). The high density of Ag nanosheets also contributes to the suppression of competitive HER, as supported by its lower H_2 selectivity (Figure 3c). In terms of CO production efficiency, the Ag FS-HF electrode delivered a partial current density of CO

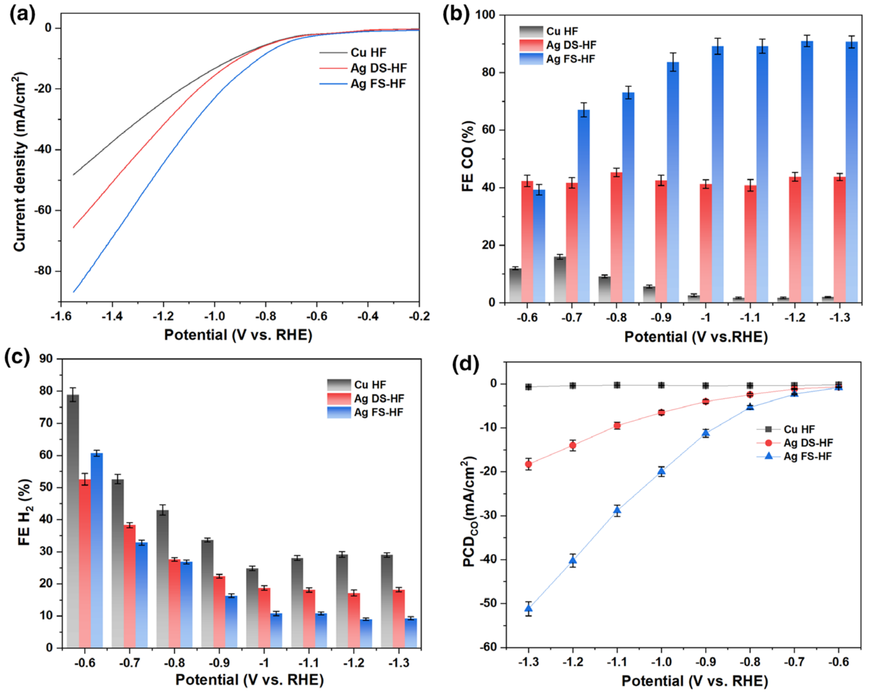

Figure 3. a) Linear sweep voltammetry (LSV) curve, b) Faradaic efficiency of CO, c) H_2, and d) partial current density of CO over Cu HF, Ag DS-HF, and Ag FS-HF electrodes.

(PCD_{CO}) of 51.2 mA cm^{-2} at −1.3 (V vs RHE), significantly outperforming the Cu HF electrode (Figure 3d). Compared to the state-of-the-art silver-based electrocatalysts, the Ag FS-HF electrode delivered a high PCDco of 41.2 and maintained a high Faradic efficiency over 91% for CO production at −1.2 (V vs RHE). In contrast, most of these electrocatalysts only achieve PCDco below 10 mA cm^{-2}. This is because the CO_2 supply is limited by dissolved CO_2 in the bulk electrolytes.

The growth of silver catalysts onto bare Cu HF significantly enhances ECSA, promotes ET, and reduces charge transfer resistance. The ECSA, evaluated via double-layer capacitance (Cdl) measurements, reveals that the Ag FS-HF electrode exhibits nearly twice the Cdl value of the Cu HF electrode (**Figure** 4a), indicating a substantially increased number of active sites. Furthermore, electrochemical impedance spectroscopy (EIS) conducted at −0.9 (V vs RHE) shows a markedly low charge transfer resistance of 6.95 Ω for the Ag FS-HF electrode, suggesting reduced charge transfer resistance and enhanced reaction kinetics (Figure 4b).

Tafel analysis was performed to elucidate the kinetics of CO_2 electroreduction to CO on the Ag FS-HF electrode. The theoretical value of the Tafel slope for the first ET is 118 mV dec^{-1}, while the involvement of a proton transfer results in a Tafel slope of 59 mV dec^{-1}.[40,41] The Ag FS-HF electrode exhibited a Tafel slope of approximately 220 mV dec^{-1}, which, while larger than the theoretical value of 118 mV dec^{-1}, suggests that the initial CO_2 activation form $*COO^-$ intermediate remains the rate-determining step. To further probe the electroreduction of CO_2 to CO mechanism on the Ag FS-HF electrode, the potential-dependent in situ Raman spectroscopy was employed. As shown in Figure 4d, two characteristic Raman peaks at around 418 and 542 cm^{-1} were detected, corresponding to surface adsorbed *COOH and $*COO^-$ intermediates.[40,41] They are key intermediates for the electrochemical conversion of CO_2 to CO, supporting a proton-electron-coupled transfer mechanism that governs the reaction pathway. The peak intensity of *COOH and $*COO^-$ increased at more negative potentials, reflecting higher surface adsorption of intermediates consistent with the observed CO_2RR activity trend (Figure 3d).

The electrochemical reduction of CO_2 to CO is generally accepted to proceed through three reaction steps as in the following Equations (1–3),

$$CO_2\,(aq) + [H^+ + e^-] \rightarrow COOH^*\,(aq) \tag{1}$$

$$COOH^*\,(aq) + [H^+ + e^-] \rightarrow CO^*\,(aq) + H_2O\,(aq) \tag{2}$$

$$CO^*\,(aq) \rightarrow CO\,(g) \tag{3}$$

A proposed mechanism for CO_2RR to CO on the Ag FS-HF electrode is illustrated in Figure 4e. The reaction initiates with CO_2 adsorption and activation on the Ag surface, leading to the formation of the $*COO^-$ intermediate, which is identified as the rate-determining step. The $*COO^-$ intermediate subsequently reacts with a proton to form the *COOH species. A subsequent proton-coupled electron transfer transforms *COOH to H_2O and *CO. Finally, *CO desorbs from the electrode, releasing CO gas and regenerating the active sites for the next catalytic cycle.

2.3. HFGDE Configuration and the Evaluation at Industrial-Level Current Density

At industrial-level current densities, the rapid consumption of CO_2 near the catalytic sites can lead to local CO_2 depletion, which promotes competing side HER and compromises CO_2 to CO electroreduction.[18,21] Thus, maintaining adequate CO_2 availability at the reaction interface is essential for suppressing HER and sustaining efficient CO_2RR efficiency under such conditions. In the flow-through gas diffusion electrode configuration (**Figure** 5a; Figure S8a, Supporting Information), CO_2 is introduced through the lumen side of the hollow fiber electrode, with the opposite end sealed. This setup allows CO_2 to penetrate through the porous fiber walls and directly reach the catalyst/electrolyte interface. The computational fluid dynamics (CFD) modeling visualized the CO_2 distribution on D-AgNS HF in GDE mode (Figure S8b, Supporting Information), where the CO_2 continuously flows through the hollow fiber micron-scale channels, efficiently reaching the catalyst-electrolyte interfaces. In contrast, in the non-GDE mode, CO_2 gas is bubbled into the bulk catholyte, resulting in pore flooding within electrodes (Figure 5b; Figure S8c, Supporting Information). This significantly limits CO_2 mass transport due to the extended diffusion path from the electrolytes to the active sites (Figure S8d, Supporting Information), thereby reducing overall CO_2RR performance.[42]

At industrial-level current densities, competition for electrons between CO_2 and water intensifies. When CO_2 is adequately supplied via the electrode (Figure 5a), the electroreduction of CO_2 to CO is

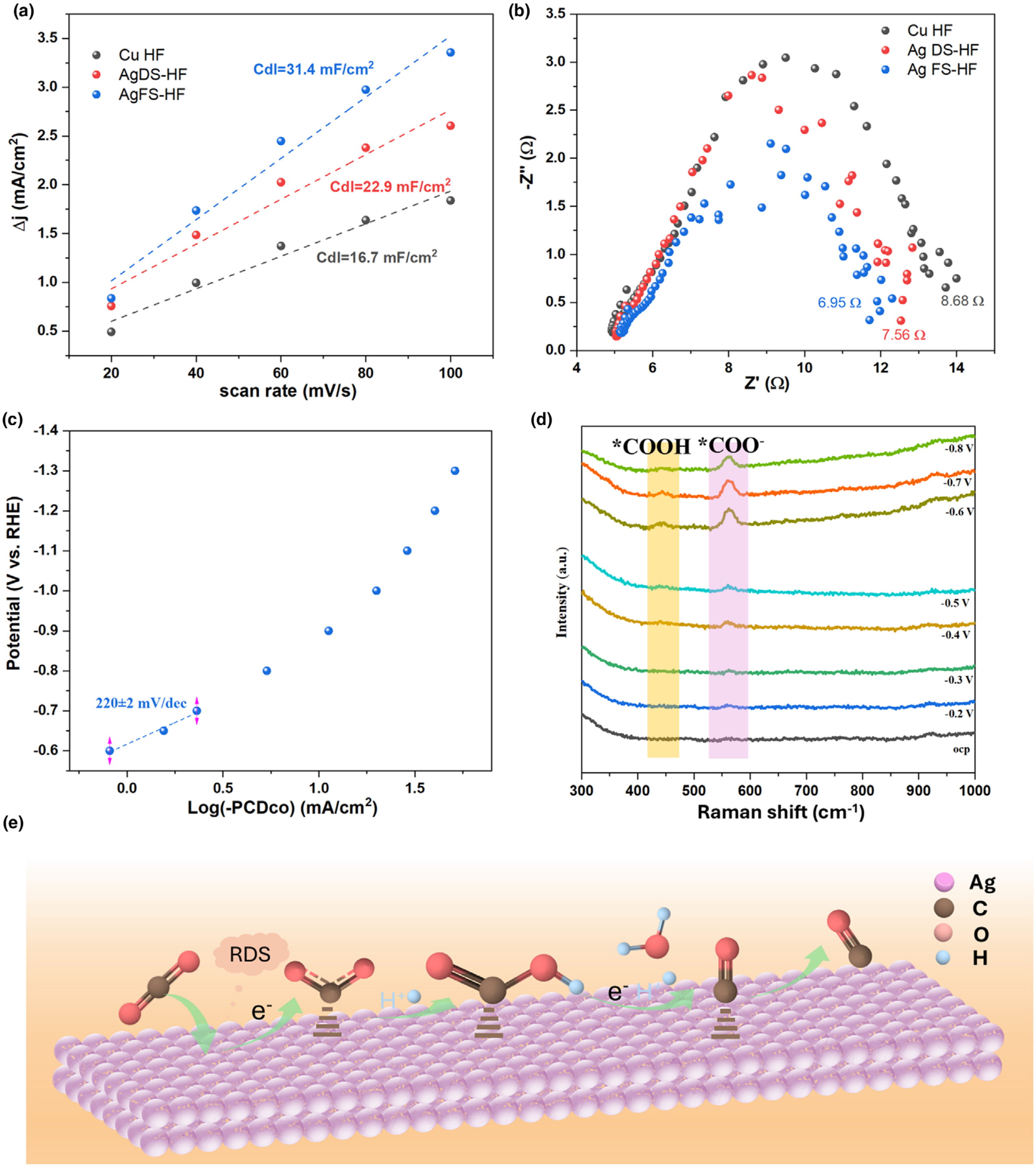

Figure 4. a) Dual-layer capacitance values of Cu HF, Ag DS-HF, and Ag FS-HF electrodes; b) electrochemical impedance spectroscopy (EIS) Nyquist plot over Cu HF, Ag DS-HF, and Ag FS-HF electrodes measured at −0.9 (V vs RHE); c) Tafel slope analysis of Ag FS-HF electrode; d) time-resolved operando Raman spectra to monitor CO$_2$RR intermediates at applied potentials over Ag FS-HF electrode; e) proposed reaction pathway for electrochemical reduction of CO$_2$ to CO on the Ag FS-HF electrode surface.

favored. However, insufficient CO$_2$ availability at active site shifts the reaction selectivity toward HER (Figure 5b). This trend is reflected in the Faradaic efficiency of CO (FE CO) under GDE and non-GDE operating modes (Figure 5c). When operating in non-GDE mode, FE CO decreased sharply to 25.2% at 100 mA cm^{-2} to just 8.1% at 400 mA cm^{-2}. In contrast, the Ag FS-HF electrode in GDE mode

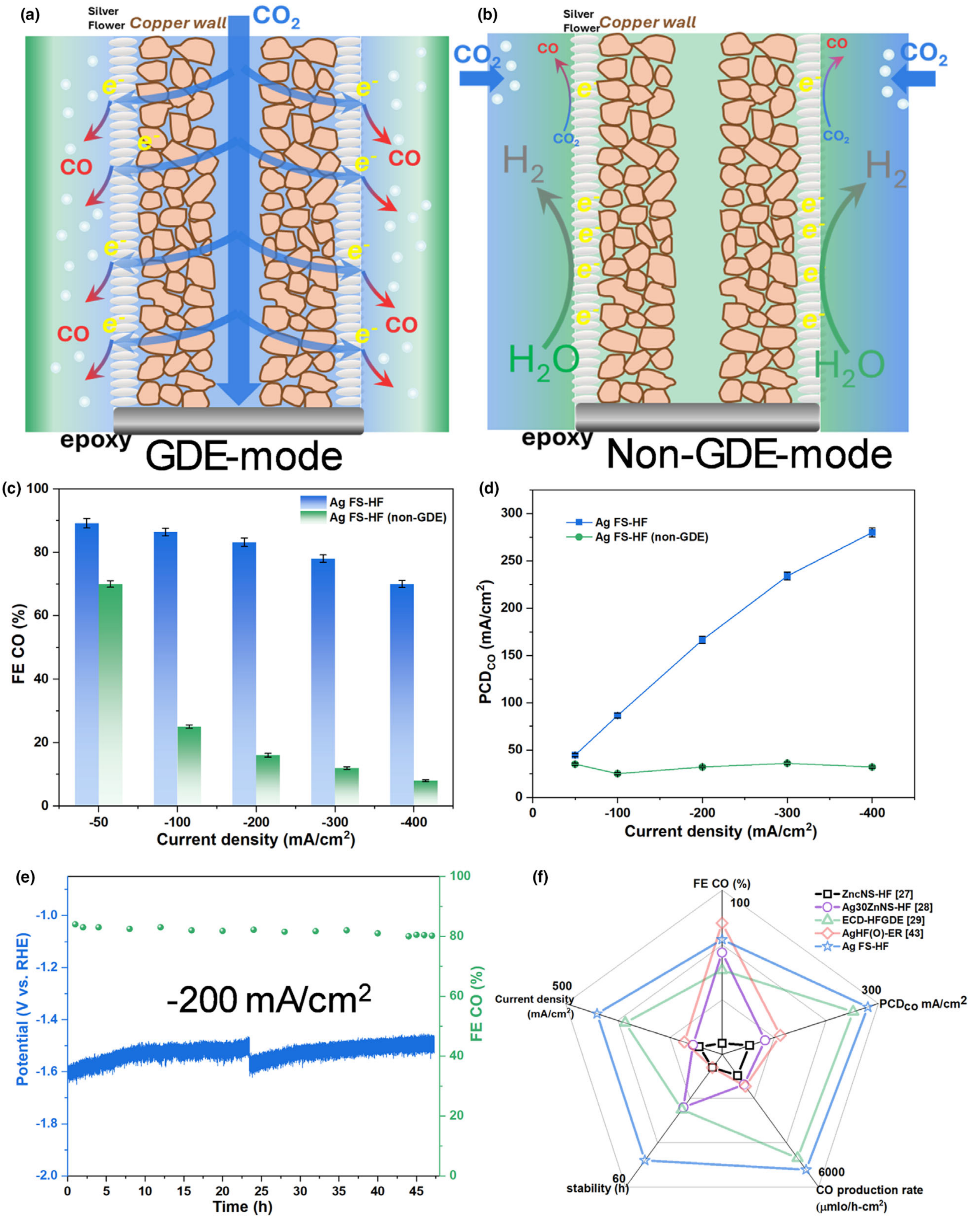

Figure 5. Schematic illustration of CO_2 and water distribution for Ag FS-HF electrode operated in a) GDE mode and b) non-GDE mode; c) Faradaic efficiency of CO and d) partial current density of CO (PCD_{CO}) for Ag FS-HF electrode performed in GDE and non-GDE mode at applied current densities; e) long-term operation of Ag FS-HF electrode in customized flow cell at $-200\ \mathrm{mA\ cm^{-2}}$; f) overall CO_2RR performance comparison for peer HFGDEs including ZncNS-HF,[27] Ag30ZnNS-HF,[28] ECD-HFGDE,[29] AgHF(O)-ER,[43] and Ag FS-HF electrodes.

maintained significantly higher FE CO values of 86.4% and 70.2% at the corresponding current densities. In terms of H_2 formation, the Ag FS-HF electrode in GDE mode exhibited a Faradaic efficiency of H_2 below 30%, whereas non-GDE operation resulted in a significantly higher FE of H_2 exceeding 88% (Figure S9, Supporting Information).

In GDE mode, the Ag FS-HF electrode achieved a PCD_{CO} as high as 280.0 mA cm^{-2} and a CO production rate of 5223.1 μmol h·cm^{-2}, an order of magnitude higher than only 32.1 mA cm^{-2} and 596.9 μmol h·cm^{-2} observed in non-GDE mode (Figure 5d; Figure S10, Supporting Information). Notably, the ratio of PCD_{CO} in GDE to non-GDE mode exhibited a significant increase with current density, rising from 1.3 at 50 to 3.5 at 100 mA cm^{-2}, further to 8.8 at 400 mA cm^{-2} (Figure S11, Supporting Information). These results highlight that at industrial-level current densities, the reaction of CO_2 electroreduction is governed by the availability of CO_2 at active sites. A continuous and sufficient CO_2 supply enabled by the flow-through GDE configuration is therefore essential to suppress HER and maintain CO_2RR performance.[44,45]

The long-term stability testing of the Ag FS-HF electrode was carried out in a customized flow cell (Figure S12, Supporting Information), using 1 M KCl with 0.1 M $KCHO_3$ buffer as the catholyte under a constant current density of 200 mA cm^{-2}. The Ag FS-HF electrode exhibited excellent durability (Figure 5c), maintaining a FE CO around 80% during 47 h with refreshing electrolytes after 24 h. Post-stability XRD analysis confirmed the structural integrity of the Ag catalyst layer with Cu HF (Figure S13, Supporting Information). The SEM image of the related electrode (Figure S14, Supporting Information) further revealed that the flower structure with a high density of thin Ag nanosheets remained intact after long-term testing, reflecting the robust performance of the Ag catalyst. Furthermore, quantitative XPS analysis (Figure S15, Supporting Information) revealed a surface atomic ratio of Ag to Cu for Ag FS-HF (after reaction) of 97.9:2.1, similar to that of Ag FS-HF before reaction (Table S1, Supporting Information), indicating the robustness of the silver catalyst layer. A comparison between the Ag FS-HF electrode and previously reported HFGDEs[27–29,43] further highlights its superior performance (Figure 5f). Notably, the Ag FS-HF electrode delivered exceptional stability, maintaining continuous electroreduction of CO_2 to CO over 47 h at 200 mA cm^{-2}, significantly outperforming the reported ZncNS-HF electrode.[27] This indicates the in situ galvanic growth of silver catalysts offers greater structural robustness and interfacial integrity compared to electrodeposited Zn catalysts on Cu HF. Furthermore, the Ag FS-HF electrode also achieved the highest PCD_{CO} and CO production rate, attributed to the synergistic effect of its densely packed, ultrathin Ag nanosheets and the flow-through GDE configuration, which together facilitate efficient CO_2 transport to the catalytic sites, thereby enhancing CO_2RR activity under industrially relevant conditions.

3. Conclusion

In this study, we applied a simple galvanic replacement method to in situ-grown highly active silver flower-like catalyst on Cu HFGDEs to tune its selectivity for the electrochemical reduction of CO_2 to CO. The formation of high-density Ag nanosheet-based flower-like structures was delivered through the synergistic action of citric acid and ammonia during the GRR between Ag^+ and Cu. The resulting Ag FS-HF electrode achieved nearly twice the ESCA and current density as that of the bare Cu HF. The Ag FS-HF electrode also delivered a high Faradaic efficiency of CO of 91% at −1.2 (V vs RHE). The dense coverage of the Ag flower structure is key to preventing the underlying Cu substrate from participating in the reaction, whereas the Ag DS-HF, which exposes some of the Cu surface, leads to the formation of formate. In situ Raman spectroscopy revealed that the highly active Ag flower structure enhanced the adsorption of the *COOH intermediate, facilitating CO_2RR kinetics. At industrial-level current density, the Ag FS-HF electrode achieved a partial current density of CO of 280.8 mA cm^{-2}, attributed to the HFGDE configuration ensuring sufficient CO_2 delivery to the active sites. The ratio of PCD_{CO} in GDE mode versus non-GDE mode increased significantly with current density, underscoring the critical role of CO_2 availability in suppressing HER and maintaining CO_2RR activity. The Ag FS-HF electrode delivered exceptional stability, maintaining continuous electroreduction of CO_2 to CO over 47 h at 200 mA cm^{-2}, indicating the in situ galvanic growth of silver catalysts offers greater structural robustness and interfacial integrity. This work highlights a promising strategy for the rational design of flow-through GDEs to maximize desired conversion under industrially relevant conditions. Beyond the electrochemical conversion of CO_2 to CO, the hollow fiber electrode can serve as a versatile platform for targeting other CO_2RR production (e.g., formate and ethanol) or other gas-phase reactions (e.g., electroreduction of N_2, CO) by tailoring catalyst selectivity. However, the complex fabrication process leads to poor pore size distribution. Future studies can look forward to tuning pore sizes, ensuring consistent gas permeability, and maximizing the triple-phase interfaces.

Acknowledgements

We acknowledge financial support from the ARC Future Fellowship (FT220100166), Discovery project (DP190101782), ARC LIEF grant (No. LE230100179), and Centre of Excellence for Green Electrochemical Transformation of Carbon Dioxide (CE230100017). Open access publishing facilitated by University of Southern Queensland, as part of the Wiley - University of Southern Queensland agreement via the Council of Australian University Librarians.

Conflict of Interest

The authors declare no conflict of interest.

Supporting Information

Supporting Information is available from the Wiley Online Library or from the author.

Keywords

electrochemical CO_2 reduction, galvanic replacement reaction, gas diffusion electrodes, hollow fiber, silver catalysts

Received: July 17, 2025
Revised: October 5, 2025
Published online: October 14, 2025

---

[1] P. De Luna, C. Hahn, D. Higgins, S. A. Jaffer, T. F. Jaramillo, E. H. J. S. Sargent, *Science* **2019**, *364*, eaav3506.
[2] S. Cao, S. Zhou, H. Chen, S. Wei, S. Liu, X. Lin, X. Chen, Z. Wang, W. Guo, X. Lu, *Energy Environ. Mater.* **2022**, *6*, e12287.

[3] F. P. García de Arquer, C.-T. Dinh, A. Ozden, J. Wicks, C. McCallum, A. R. Kirmani, D.-H. Nam, C. Gabardo, A. Seifitokaldani, X. J. S. Wang, *Scinece* **2020**, *36*, 661.

[4] R. S. J. S. Haszeldine, *Science* **2009**, *325*, 1647.

[5] J. E. Huang, F. Li, A. Ozden, A. Sedighian Rasouli, F. P. García de Arquer, S. Liu, S. Zhang, M. Luo, X. Wang, Y. J. S. Lum, *Science* **2021**, *372*, 1074.

[6] W. J. Teh, M. J. Kolb, F. Calle-Vallejo, B. S. J. A. F. M. Yeo, *Adv. Funct. Mater.* **2022**, *33*, 2210617.

[7] H. Rabiee, B. Ma, Y. Yang, F. Li, P. Yan, Y. Wu, X. Zhang, S. Hu, H. Wang, L. J. A. F. M. Ge, *Adv. Funct. Mater.* **2025**, *35*, 2411195.

[8] Y. Liu, Z. Wei, X. Su, X. Shi, L. Liu, T. Wang, X. Xu, M. Zhao, Y. Zhai, H. B. J. A. F. M. Yang, *Adv. Funct. Mater.* **2025**, *35*, 2403547.

[9] Z. Yang, H. Wang, X. Bi, X. Tan, Y. Zhao, W. Wang, Y. Zou, H. Wang, H. Ning, M. Wu, *Energy Environ. Mater.* **2023**, *7*, e12508.

[10] L. Xiao, R. Zhou, T. Zhang, X. Wang, R. Zhou, P. J. Cullen, K. Ostrikov, *Energy Environ. Mater.* **2023**, *7*, e12656.

[11] A. Raya-Imbernón, A. A. Samu, S. Barwe, G. Cusati, T. s. Fődi, B. M. Hepp, C. J. A. E. L. Janáky, *ACS Energy Lett.* **2023**, *9*, 288.

[12] N. T. Nesbitt, T. Burdyny, H. Simonson, D. Salvatore, D. Bohra, R. Kas, W. A. J. A. C. Smith, *ACS Catal.* **2020**, *10*, 14093.

[13] Z. Wang, Y. Zhou, P. Qiu, C. Xia, W. Fang, J. Jin, L. Huang, P. Deng, Y. Su, R. J. A. M. Crespo-Otero, *Adv. Mater.* **2023**, *35*, 2303052.

[14] Y. Kuang, H. Rabiee, L. Ge, T. E. Rufford, Z. Yuan, J. Bell, H. Wang, *Energy Environ. Mater.* **2023**, *6*, e12596.

[15] S. Garg, M. Li, A. Z. Weber, L. Ge, L. Li, V. Rudolph, G. Wang, T. E. Rufford, *J Mater Chem A* **2020**, *8*, 1511.

[16] S. Jin, Z. Hao, K. Zhang, Z. Yan, J. Chen, *Angew. Chem. Int. Ed. Engl.* **2021**, *60*, 20627.

[17] D. Wu, F. Jiao, Q. Lu, *ACS Catal.* **2022**, *12*, 12993.

[18] Q. Sun, C. Jia, H. Lu, M. Yang, R. Liu, D. M. Villamanca, Y. Zhao, C. Zhao, *Chem. Soc. Rev.* **2025**, *54*, 6973.

[19] H. Rabiee, L. Ge, X. Zhang, S. Hu, M. Li, Z. Yuan, *Energy Environ. Sci.* **2021**, *14*, 1959.

[20] H. Rabiee, L. Ge, S. Hu, H. Wang, Z. Yuan, *Chem. Eng. J.* **2022**, *450*, 138476.

[21] G. Chen, H. Rabiee, M. Li, B. Ma, Y. Kuang, F. Dorosti, Z. Zhu, H. Wang, L. Ge, *Adv. Mater.* **2025**, *37*, e2420391.

[22] R. Kas, K. K. Hummadi, R. Kortlever, P. de Wit, A. Milbrat, M. W. Luiten-Olieman, N. E. Benes, M. T. Koper, G. Mul, *Nat. Commun.* **2016**, *7*, 10748.

[23] D. Liu, Y. Hu, E. Shoko, H. Yu, T. T. Isimjan, X. Yang, *Electrochim. Acta* **2021**, *365*, 137343.

[24] C. Zhu, G. Shen, W. Chen, X. Dong, G. Li, Y. Song, W. Wei, Y. Sun, *J. Power Sources* **2021**, *495*, 229814.

[25] C. Zhu, Y. Song, X. Dong, G. Li, A. Chen, W. Chen, G. Wu, S. Li, W. Wei, Y. Sun, *Energy Environ. Sci.* **2022**, *15*, 5391.

[26] C. Zhu, G. Wu, J. Mao, A. Chen, Y. Zhao, G. Feng, Y. Wei, X. Liu, S. Li, G. Li, X. Dong, Y. Song, W. Wei, W. Chen, *Chem. Eng. J.* **2024**, *485*, 150040.

[27] G. Chen, L. Ge, Y. Kuang, H. Rabiee, B. Ma, F. Dorosti, A. Kumar Nanjundan, Z. Zhu, H. Wang, *Chem. Eng. J.* **2024**, *490*, 151651.

[28] G. Chen, L. Ge, Y. Kuang, H. Rabiee, B. Ma, F. Dorosti, A. K. Nanjundan, Z. Zhu, H. Wang, *Small Sci.* **2024**, *4*, 2400184.

[29] G. Chen, L. Ge, B. Ma, Y. Kuang, H. Rabiee, F. Dorosti, A. K. Nanjundan, Z. Zhu, H. Wang, *Appl. Catal. B Environ. Energy* **2025**, *363*, 124803.

[30] Z. Meng, F. Wang, Z. Zhang, S. Min, *Nanoscale* **2024**, *16*, 2295.

[31] H. Rabiee, L. Ge, X. Zhang, S. Hu, M. Li, S. Smart, Z. Zhu, Z. Yuan, *Appl. Catal. B Environ.* **2021**, *286*, 119945.

[32] H. Rabiee, L. Ge, J. Zhao, X. Zhang, M. Li, S. Hu, S. Smart, T. E. Rufford, Z. Zhu, H. Wang, Z. Yuan, *Appl. Catal. B Environ.* **2022**, *310*, 121362.

[33] H. Rabiee, X. Zhang, L. Ge, S. Hu, M. Li, S. Smart, Z. Zhu, Z. Yuan, *ACS Appl. Mater. Interfaces* **2020**, *12*, 21670.

[34] S. Watmanee, T. Klinaubol, R. Nganglumpoon, P. Pinthong, A. R. Christian Serraon, M. Chionglii, Y. Morikawa, J. Panpranot, *Chem. Eng. J.* **2024**, *480*, 148182.

[35] X. Wu, Y. Guo, Z. Sun, F. Xie, D. Guan, J. Dai, F. Yu, Z. Hu, Y. C. Huang, C. W. Pao, J. L. Chen, W. Zhou, Z. Shao, *Nat. Commun.* **2021**, *12*, 660.

[36] S. Yan, S. A. Mahyoub, J. Lin, C. Zhang, Q. Hu, J. Zhong, C. Chen, F. Zhang, Z. Cheng, *J. Catal.* **2022**, *405*, 224.

[37] X. Li, X. Lin, B. Liu, X. Zhao, H. Zhao, L. Wang, S. Cong, *Appl. Phy. A* **2019**, *12*, 492.

[38] Y. Xia, Y. Wu, T. Hang, J. Chang, M. Li, *Langmuir* **2016**, *32*, 3385.

[39] S. Yang, D. Slotcavage, J. D. Mai, F. Guo, S. Li, Y. Zhao, Y. Lei, C. E. Cameron, T. J. Huang, J. Mater, *Chem. C* **2014**, *2*, 8350.

[40] S. Li, W. Chen, X. Dong, C. Zhu, A. Chen, Y. Song, G. Li, W. Wei, Y. Sun, *Nat. Commun.* **2022**, *13*, 3080.

[41] S. Li, X. Dong, J. Mao, W. Chen, A. Chen, G. Wu, C. Zhu, G. Li, Y. Wei, X. Liu, J. Wang, Y. Song, W. Wei, *Small* **2023**, *19*, e2301338.

[42] Y. Kuang, G. Chen, D. H. Mudiyanselage, H. Rabiee, B. Ma, F. Dorosti, A. K. Nanjundan, Z. Zhu, H. Wang, L. Ge, *Chem. Eur. J.* **2024**, *30*, e202403251.

[43] Y. Kuang, G. Chen, H. Rabiee, B. Ma, F. Dorosti, A. K. Nanjundan, Z. Zhu, H. Wang, L. Ge, *Energy Fuel* **2024**, *38*, 10096.

[44] B. Ma, H. Rabiee, G. Chen, Y. Kuang, T. Zhu, P. Yan, L. Ge, Z. Zhu, *Chem. Eng. J.* **2025**, *523*, 168323.

[45] G. Chen, M. Hong, B. Ma, Y. Kuang, H. Rabiee, X. Xu, F. Dorosti, P. Yan, N. Shah, A. K. Nanjundan, Z. Zhu, H. Wang, L. Ge, *Appl. Catal. B Environ. Energy* **2026**, *381*, 125902.